EXIRAD-HE
Multi-pinhole high-resolution ex vivo imaging of high-energy isotopes

Nguyen, Minh Phuong; Goorden, Marlies C.; Beekman, Freek J.

DOI
10.1088/1361-6560/abbb77

Publication date
2020

Document Version
Final published version

Published in
Physics in Medicine and Biology

Citation (APA)
Nguyen, M. P., Goorden, M. C., & Beekman, F. J. (2020). EXIRAD-HE: Multi-pinhole high-resolution ex vivo imaging of high-energy isotopes. *Physics in Medicine and Biology*, *65*(22), Article 225029. https://doi.org/10.1088/1361-6560/abbb77

Physics in Medicine & Biology

IPEM Institute of Physics and Engineering in Medicine

EXIRAD-HE: multi-pinhole high-resolution *ex vivo* imaging of high-energy isotopes

To cite this article: Minh Phuong Nguyen *et al* 2020 *Phys. Med. Biol.* **65** 225029

IOP Publishing Phys. Med. Biol. 65 (2020) 225029 https://doi.org/10.1088/1361-6560/abbb77

Physics in Medicine & Biology

IPEM Institute of Physics and Engineering in Medicine

OPEN ACCESS

RECEIVED
4 July 2020

REVISED
8 September 2020

ACCEPTED FOR PUBLICATION
24 September 2020

PUBLISHED
18 November 2020

PAPER

EXIRAD-HE: multi-pinhole high-resolution *ex vivo* imaging of high-energy isotopes

Minh Phuong Nguyen[1], **Marlies C Goorden**[1] and **Freek J Beekman**[1,2,3]

[1] Section of Biomedical Imaging, Faculty of Applied Sciences, Delft University of Technology, Mekelweg 15, Delft, JB, 2629, The Netherlands
[2] MILabs B.V., Heidelberglaan 100, Utrecht, CX, 3584, The Netherlands
[3] Department of Translational Neuroscience, Brain Center Rudolf Magnus, University Medical Center Utrecht, The Netherlands

E-mail: m.p.nguyen@tudelft.nl

Keywords: multi-pinhole, SPECT, ex vivo, high-energy isotope, tissue sample

Abstract

We recently developed a dedicated focusing multi-pinhole collimator for a stationary SPECT system that offers down to 120 μm (or 1.7 nL) spatial resolution SPECT images of cryo-cooled tissue samples (EXIRAD-3D). This collimator is suitable for imaging isotopes that are often used in small animal and diagnostic SPECT such as ^{125}I (27 keV), ^{201}Tl (71 keV), $^{99\mathrm{m}}$Tc (140 keV), and ^{111}In (171 and 245 keV). The goal of the present work is to develop high-resolution pinhole imaging of tissue samples containing isotopes with high-energy photon emissions, for example, therapeutic alpha and beta emitters that co-emit high energy gammas (e.g. ^{213}Bi (440 keV) and ^{131}I (364 keV)) or 511 keV annihilation photons from PET isotopes. To this end, we optimise and evaluate a new high energy small-bore multi-pinhole collimator through simulations. The collimator-geometry was first optimised by simulating a Derenzo phantom scan with a biologically realistic activity concentration of ^{18}F at two system sensitivities (0.30% and 0.60%) by varying pinhole placements. Subsequently, the wall thickness was selected based on reconstructions of a Derenzo phantom and a uniform phantom. The obtained collimators were then evaluated for ^{131}I (364 keV), ^{213}Bi (440 keV), ^{64}Cu (511 keV), and ^{124}I (511 + 603 keV) with biologically realistic activity concentrations, and also for some high activity concentrations of ^{18}F, using digital resolution, mouse knee joint, and xenograft phantoms. Our results show that placing pinhole centres at a distance of 8 mm from the collimator inner wall yields good image quality, while a wall thickness of 43 mm resulted in sufficient shielding. The collimators offer resolutions down to 0.35 mm, 0.6 mm, 0.5 mm, 0.6 mm, and 0.5 mm when imaging ^{131}I, ^{213}Bi, ^{18}F, ^{64}Cu, and ^{124}I, respectively, contained in tissue samples at biologically achievable activity concentrations.

1. Introduction

Preclinical imaging of radiolabeled molecule distributions in small animals plays an important role in studying the mechanisms of disease and developing diagnostic tracers (Rowland and Cherry 2008). A wide and steadily increased variety of tracers with different radioisotopes is available. While conventional SPECT scanners are designed to image isotopes emitting gammas with a typical energy of around 140 keV, many available and emerging isotopes emit gammas with higher energies. These include PET tracers that emit 511 keV annihilation photons (e.g. ^{18}F, ^{124}I, and ^{64}Cu), and alpha or beta emitters for theranostic applications that co-emit high-energy gammas (e.g. ^{131}I, ^{213}Bi, and ^{209}At). Many commercial preclinical PET scanners for imaging positron emitters have been launched. Recent ones include Mediso NanoPET/CT (Herrmann *et al* 2013), Bruker Albira (Gonzalez *et al* 2016), Clairvivo (Sato *et al* 2016), and Molecubes β-CUBE (Krishnamoorthy *et al* 2018), which achieve resolutions down to approximately 0.9 mm. With one small field-of-view (FOV) prototype coincidence system, a resolution of 0.6 mm was obtained (Yang *et al* 2016).

In another approach, PET isotopes are successfully imaged using dedicated clustered multi-pinhole collimators in a triangular detector set up (VECTor) at an initial resolution of < 0.75 mm *in vivo* for ^{18}F

(Goorden *et al* 2013, Walker *et al* 2014, Gonzalez *et al* 2016). Today resolutions of commercial VECTor scanners are < 0.6 mm for ^{18}F simultaneously with 0.4 mm resolution ^{99m}Tc imaging. Compared to coincidence PET, multi-pinhole PET effectively removes or reduces several image degrading effects that significantly limit the image quality in small animals. These include limited detector resolution and depth-of-interaction effects whose influence can be strongly diminished by pinhole magnification, as well as non-collinearity of annihilation photons, and random coincidences which do not play a role in pinhole PET. As a result, the resolution of VECTor can outperform coincidence PET in a subset of imaging situations (Walker *et al* 2014). In addition, with VECTor, the prompt gammas that are emitted by some PET isotopes (e.g. 603 keV for ^{124}I) can be employed to exclude the effect of positron range that sets a fundamental limit on the resolution in coincidence PET. This enables for example 0.75 mm resolution PET of ^{124}I and ^{89}Zr (Beekman *et al* 2018, Beekman *et al* 2020) as well as multi-isotope PET. At the same time, VECTor has the capability of sub-mm resolution imaging of isotopes that emit single gammas above the conventional SPECT energy range like ^{131}I (364 keV), ^{213}Bi (440 keV), and ^{209}At (545 keV) (de Swart *et al* 2016, van der Have *et al* 2016, Crawford *et al* 2018). Therefore, multi-pinhole imaging is a single-system solution for high-resolution imaging of gamma- and positron-emitting isotopes over a broad energy range.

One way to improve the resolution-sensitivity trade-off of tissue samples in pinhole SPECT and PET is to increase the pinhole magnification factor by decreasing the collimator's FOV. This concept was used for the *ex vivo* imaging technique EXIRAD-3D (MILabs B.V.), which was designed for low and medium energy isotopes such as ^{125}I (27 keV), ^{201}Tl (71 keV), ^{99m}Tc (140 keV), and ^{111}In (171 keV and 245 keV) (Nguyen *et al* 2019, 2020). With this technique, 120 μm (or 1.7 nL) resolution was obtained for ^{99m}Tc, i.e. about a ten times better volumetric resolution than state-of-the-art *in vivo* preclinical SPECT (Ivashchenko *et al* 2014). EXIRAD-3D consists of a dedicated small FOV multi-pinhole collimator, a tissue holder connected directly to a refillable chamber with dry ice for cryo-cooling the tissue throughout the scan, and dedicated acquisition and reconstruction software.

Today, EXIRAD-3D coupled with *in vivo* imaging modules as is done in the commercial MILabs' nuclear scanners offers both longitudinal information of biological and physiological functions and extra-fine three-dimensional image details, with a direct link between the two datasets. That is achieved with little more effort than the conventional *in vivo* imaging workflow without the need for whole new equipment and a complicated tissue sectioning and handling process as in a histological study. However, note that EXIRAD-3D is only designed for imaging gamma-emitters but not pure alpha- and beta-emitters.

The aim of the present paper is to design an EXIRAD option (EXIRAD-HE) that is also suited for imaging high-energy isotopes. The approach is to use narrow pinhole opening angles to suppress pinhole edge penetration and scatter, with thick collimators walls. Full system simulations of a Derenzo phantom scan and a cylindrical phantom scan with a biologically realistic activity concentration of ^{18}F were performed for various collimator designs at two system sensitivities (0.30% and 0.60%). Best performing collimators were subsequently evaluated for ^{18}F scans with several activity concentrations and for ^{64}Cu, ^{124}I, ^{213}Bi, and ^{131}I with digital joint and xenograft phantoms.

2. Methods

2.1. Considerations in collimator design and optimisation

The EXIRAD-HE collimator (see figure 1) is designed to have the same central field-of-view (CFOV) size (4 mm diameter) and inner diameter (21 mm) as the available low-energy collimator meaning that the same size tissue volumes can be scanned by means of the scanning focus method (Vastenhouw and Beekman 2007). With this method, the tissue is moved to multiple positions inside the collimator such that the whole tissue volume is viewed by the CFOV, and acquisitions from all of the scanned positions are used together in image reconstruction. The collimator is mounted in a U-SPECT or VECTor system having a fixed triangular detector setup with three large-field-of-view gamma cameras. In this study, we assume a 9.5 mm thick NaI(Tl) crystal with a usable area of 497.4*410.6 mm^2 for each detector. The crystal surface is placed at a distance of 210 mm from the collimator's centre. The EXIRAD-HE collimator contains a large number of round knife-edge pinholes placed manually in such a way that overlapping pinhole projections are limited without using a shielding layer (see section 2.4.3). All pinholes' axes point towards the collimator's centre, and the pinholes' centres are placed at the same distance from the collimator's longitudinal axis. Collimator material assumed is a tungsten alloy consisting of 97% W, 1.5% Ni, and 1.5% Fe.

With the above-mentioned constraints, we restricted the parameters for optimisation to be the distance from the pinhole's centre to the collimator's inner surface (**h**), the pinhole diameter (**d**), and the wall thickness (**T**) (see figure 1). Other parameters as listed in table 1, if not fixed, can be expressed by these parameters. For example, pinhole opening angle only depends on **h** because the size of the CFOV (4 mm diameter sphere) and the distance from the collimator's longitudinal axis to the collimator's inner surface

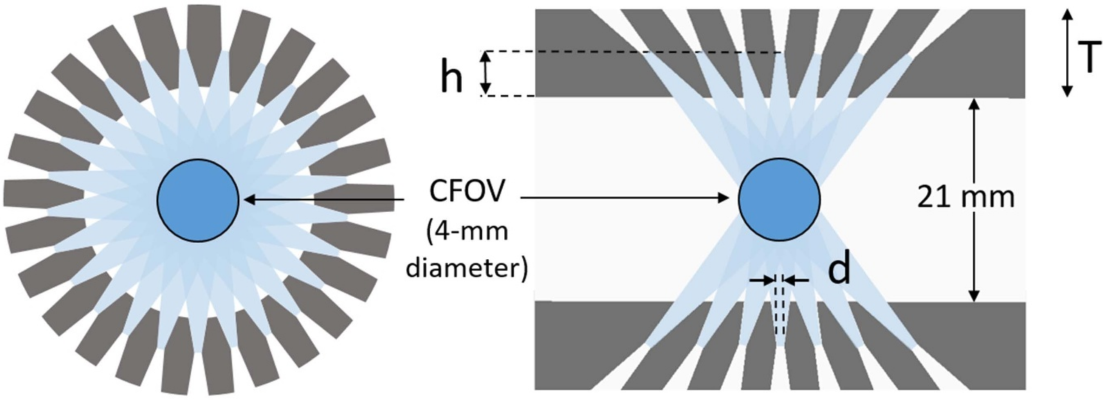

Figure 1. Sketch of the EXIRAD-HE focusing multi-pinhole collimator. Pinholes are placed in several rings and all focus on a central FOV.

(10.5 mm) were fixed. Also, the total number of pinholes were calculated from the detector size ($3 * 497.4 * 410.6$ mm^2) and the size of pinhole projections (again only depending on **h**) (see equation (3)). For the three parameters to be optimised, the following considerations were taken into account:

- For **h**, one may expect that the closer the pinhole is to the object (i.e. **h** approaches 0), the higher the system resolution that can be achieved for a fixed sensitivity (Rentmeester *et al* 2007). This suggests putting the pinhole apertures as close to the inner surface of the collimator as possible. However, putting pinholes closer gives more sensitivity per pinhole but fewer pinholes that can be placed for the same detector area, which in some cases, limits the resolution-sensitivity trade-off (Goorden *et al* 2009). Besides, for the high energy photons (e.g. 511 keV), putting pinholes closer to the inner collimator wall would result in a significant increase of pinhole edge scatter and penetration because of shorter paths that photons travel through the pinhole edges, which deteriorates image quality. Thus an intermediate value for **h** may be most beneficial.
- The pinhole diameter **d** directly decides the resolution-sensitivity trade-off of the system: reducing the pinhole diameter improves the resolution at the expense of decreasing the sensitivity and vice versa.
- For **T**, we would expect that the larger the wall thickness, the better prevention of direct collimator wall penetration which is important for image quality. However, the thicker the collimator, the heavier and more expensive the collimator is which limits its practical use as a final product.

It is not straightforward to find an optimal set for all of these parameters analytically. We, therefore, utilised an analytical model for the initial estimate of the parameter sets, and then our optimisation was based on evaluating the quality of the final reconstructed images obtained from Monte Carlo Simulation (MCS) data. The following sections will explain this process in more detail.

2.2. Analytical model

The analytical model was used for ^{18}F (511 keV), and we only optimised the collimator for this energy, which lies inside the studied energy range (364–603 keV). For the initial optimisation, we used an analytical model which is based on the models in (Metzler *et al* 2001, Rentmeester *et al* 2007) that can efficiently predict the performance of multi-pinhole SPECT and has been applied in optimising a small-animal SPECT system, namely U-SPECT-I (Beekman *et al* 2005), as well as in a theoretical analysis of a human brain SPECT (Goorden *et al* 2009). It models collimator and detectors as spherical layers surrounding the scanned object (figure 2(a)). The parameters used in this model are included in table 1.

To approximate the cylindrical collimator and the triangularly-placed detectors in EXIRAD-HE by the spherical layers in the analytical model, the average distance from the pinholes' centres and the detector surface to the collimator's centre were set as the radius of the collimator layer (r_c) and the radius of the detector layer (r_d), respectively. To this end, we sampled uniformly on each detector's surface a set of $50*50 = 2500$ points (**D**) from each of which a line was drawn through the collimator's centre. Intersections (**C**) of these lines with the cylindrical surface that goes through all pinholes' centres were calculated. Then, r_d (or r_c) was set as the average distance from **D** (or **C**) to the collimator's centre. Consequently, r_d was 278 mm as the detectors were fixed, and r_c depended on the real distance from pinholes' centres to the collimator centre (which is different for the various collimators we considered).

With the analytical model, we calculated the sensitivity over the whole CFOV instead of the peak sensitivity calculated at the collimator's centre as was done in (Rentmeester *et al* 2007). To this end, we took

Table 1. List of parameters in EXIRAD-HE.

Parameter	Description	Value
h	Distance from the pinhole's centre to the collimator's inner surface	**To be optimised**
d	Pinhole diameter	**To be optimised**
T	Wall thickness	**To be optimised**
D_x, D_z	Dimensions of each detector	497.4 mm, 410.6 mm
R_b	The radius of the collimator's bore	10.5 mm
r_d	The radius of the detector layer	278 mm
r_c	The radius of the collimator layer	Depends on **h**
r_f	The radius of the CFOV	2 mm
α	Pinhole opening angle	$2^*\arcsin(r_f/r_c)$
N	Total number of pinholes	See equation (3)
ϵ	Detector efficiency	14.3%
R_i	Detector spatial resolution	3.5 mm
μ	The attenuation coefficient of the pinhole material	See table 2
S_{CFOV}	System sensitivity over the CFOV	Initially 0.30% and 0.60%

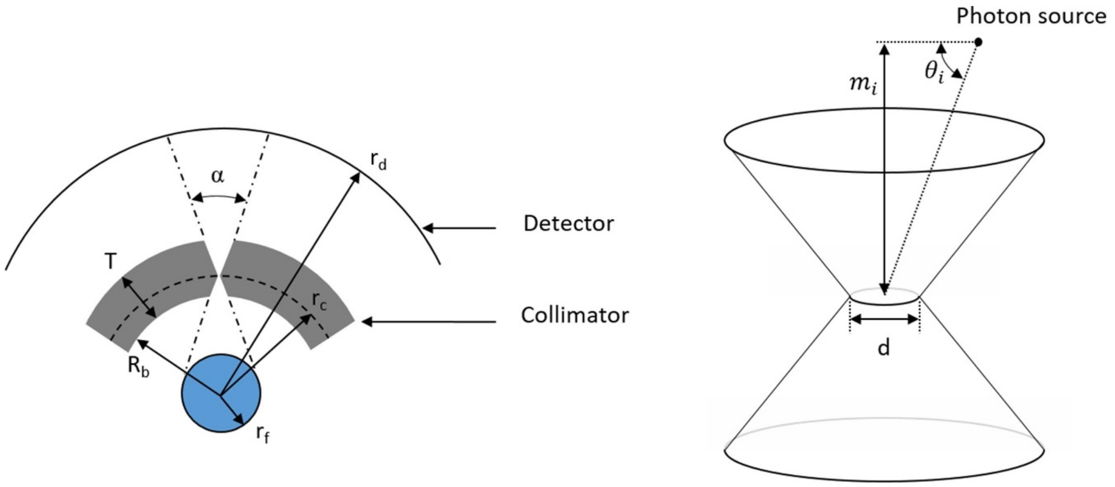

Figure 2. (a) Analytical model of the EXIRAD-HE. (b) Schematic sketch of a pinhole and a photon source for sensitivity calculation in equation (1).

the average of the sensitivities over n = 8820 points uniformly distributed within the spherical CFOV. The sensitivity at each point reads (Metzler *et al* 2001):

$$S_i = \frac{d^2 sin^3\theta_i}{16m_i^2} + \frac{sin^5\theta_i \, tan^2\frac{\alpha}{2}}{8m_i^2\mu^2}\left(1 - \frac{cot^2\theta_i}{tan^2\frac{\alpha}{2}}\right)^{\frac{1}{2}} * \left[1 - \frac{cot^2\theta_i}{tan^2\frac{\alpha}{2}} + \mu d \, csc\theta_i \, cot\frac{\alpha}{2}\right]. \tag{1}$$

where S_i is the sensitivity at photon source position i;θ_i and m_i define the location of the photon source (figure 2(b)); d is pinhole diameter; α is pinhole opening angle; μ is attenuation coefficient of the pinhole material. This average sensitivity was multiplied by the number of pinholes (N), detector efficiency (ϵ), and then multiplied by two because of the gamma pair production, to obtain the system sensitivity over the CFOV:

$$S_{CFOV} = \frac{1}{n}\sum_i S_i * N * \varepsilon * 2. \tag{2}$$

The number of pinholes was calculated as:

$$N = \frac{3 * D_X * D_Z * \pi/4}{\pi\left(\frac{r_d - r_c}{r_c} r_f\right)^2}. \tag{3}$$

This took into account that a fraction of π/4 of the total detector surface ($3 * D_X * D_Z$) is covered with non-overlapping pinhole projections. A detector photopeak efficiency ϵ of 14.3% for 511 keV was obtained from MCS, as explained in section 2.3.3. The radius of the CFOV (r_f) is 2 mm.

Table 2. Studied isotopes and corresponding simulation settings. The attenuation coefficient in collimator was obtained from NIST database (Seltzer 1993, Hubbell and Seltzer 1995), and the attenuation coefficient in the detector was calculated from MCS (section 2.3.4).

	^{18}F	^{64}Cu	^{124}I	^{213}Bi	^{131}I
Half-life	1.83 h	12.7 h	4.18 d	45.59 m	8 d
Peak energy (keV)	511	511	603	440	364
Photopeak window (keV)	460–562	460–562	543–663	396–484	328–400
Side windows (keV)	434–460 562-588	434–460 562-588	513–543 663-693	374–396 484-506	309–328 400-419
Background radiation in photopeak window	81 cps	81 cps	80 cps	84 cps	98 cps
Background radiation in two side windows	40 cps	40 cps	38 cps	42 cps	41 cps
Detector spatial resolution (mm)	3.5	3.5	3.5	3.5	3.5
Detector energy resolution (%)	9.0	9.0	8.3	9.7	10.7
Attenuation coefficient in collimator (mm^{-1})	0.250	0.250	0.204	0.309	0.420
Attenuation coefficient in detector crystal (mm^{-1})	0.012	0.012	0.010	0.017	0.025

2.3. Monte Carlo simulations

2.3.1. General settings

Geant4 Application for Tomographic Emission (GATE) (Jan *et al* 2004, 2011, Staelens *et al* 2006, Chen *et al* 2008) was used for all MCS in this research to simulate photon transport inside the scanner. Our simulation method was validated with experimental data from EXIRAD-3D with low-energy collimators in a previous publication (Nguyen *et al* 2019) where detailed settings can be found. In this work, to simulate the high-energy collimators, we adapted the following. Firstly, instead of manually defining the physics processes, here the ‘physic list builder’ mechanism was used as recommended in the recent GATE documentation, and the general ‘emstandard’ builder provided by the Geant4 community was set. This included, but was not limited to, photoelectric effect, Compton scattering, Rayleigh scattering, electron ionisation, bremsstrahlung, multiple scatter, and positron annihilation for positron emitters. Secondly, GATE’s ‘ion source’ was defined by setting the isotope’s atomic number (Z) and atomic weight (A) (e.g. $Z = 9$ and $A = 18$ for a ^{18}F source). This way, both the radioactive decay and the atomic de-excitation were incorporated, and it was straightforward to change the radioactive isotopes for different scan simulations. Finally, the detector’s spatial resolution and energy resolution were set in a different way than in (Nguyen *et al* 2019). The detector’s spatial resolution was fixed to 3.5 mm for all studied isotopes, instead of scaling it by the reciprocal of the square root of the photon’s energy which would result in a too good resolution for high energies because this way of scaling would not appropriately consider the large amount of scatter of the high-energy photons. The detector energy resolution was modelled using the inverse square law (Jan *et al* 2004), $R_{energy} = R_0\sqrt{E_0/E}$, where $\mathrm{R}_0 = 9\%$ was assumed as the full-width-at-half-maximum (FWHM) energy resolution at $\mathrm{E}_0 = 511$ keV.

After getting the projection images from the GATE output, realistic background radiation (from e.g. cosmic radiation) was added to both the photopeak window and the two side windows. This was based on the count rate from a background radiation measurement with a U-SPECT/CT system at MILabs B.V., Utrecht, the Netherlands, as reported in table 2. Table 2 also specifies the photopeak window, the side windows, and some other settings for each isotope.

2.3.2. Simulation of system sensitivity

The system sensitivity obtained from MCS was used in the collimator optimisation process to obtain pairs of **h** and **d** that would provide such sensitivity (section 2.4). Here a uniform spherical ^{18}F distribution that exactly fits inside the CFOV (4 mm diameter) and emits 10^8 positrons was simulated. The activity distribution was placed at the centre of a PMMA sphere having a diameter of 10 mm that acts as the annihilation environment. Sensitivity was calculated as the number of detected counts within the photopeak window (20%) over the number of emissions. Note that all the sensitivities reported in this work were for ^{18}F.

2.3.3. Simulation of detector efficiency

The detector efficiency was used in the analytical model. To simulate this, a uniform spherical ^{18}F source that fits in the CFOV and emits 10^8 positrons was placed at the centre of a full multi-pinhole collimator ($\mathbf{h} = 8$ mm, $\mathbf{d} = 0.27$ mm, and $\mathbf{T} = 60$ mm). The activity distribution was placed at the centre of a PMMA sphere having a diameter of 10 mm that acts as the annihilation environment. By setting the detector’s material as NaI with a normal density (3.67 g cm^{-3}) and then with a very high density (367 000 g cm^{-3}), and taking the ratio between the counts in these two cases, we obtained a detector efficiency of 14.3% for 511 keV.

2.3.4. Simulation of attenuation coefficient in detector crystal

The attenuation coefficient in the detector was simulated for each isotope and used both in the analytical model (section 2.2) and in generating the system matrix for image reconstruction (section 2.5.1). To this end, a point source containing the studied isotope that emits 10^5 photons in a beam perpendicular to one of the 9.5 mm thick NaI(Tl) scintillators was simulated. No collimator was included, and the beam was defined in GATE by the source's emission angle. Only for this simulation, the source was defined with gamma particle type and the corresponding mono-energy instead of the ion type. Subsequently, the attenuation coefficient was calculated with equation (4), and the obtained numbers are listed in table 2. This equation assumed Beer's law that did not fully include the Compton scatter (only the part that ends up being detected in the photopeak was considered); however, it provided an effective attenuation coefficient that we need for the analytical model and the system matrix generation.

$$\mu_{detector} = -\frac{1}{9.5} log\left(1 - \frac{number\ of\ detected\ photons}{10^5}\right). \tag{4}$$

2.4. Collimator optimisation and evaluation procedure

We here optimised the collimator for ^{18}F because 511 keV lies near the middle of the studied energy range (364–603 keV) and we aimed to attain a collimator that can be used for a wide energy range. The optimisation procedure was as follows:

i. First, we assumed $\mathbf{T} = 60$ mm which is significantly larger than the thickness of the available low-energy collimator for EXIRAD-3D (25.5 mm) to prevent collimator wall penetration by the high-energy photons. The probability that 511 keV photons pass through a 60 mm thick collimator material of 97% W, 1.5% Ni, and 1.5% Fe is $3.1 * 10^{-5}$%.
ii. For a fixed sensitivity averaged over the CFOV (S_{CFOV}) of either 0.30% (sensitivity of an available *in vivo* high-energy collimator in VECTor (Goorden *et al* 2013)) or double that, 0.60%, **h** was varied from 0 mm to 10 mm with a step size of 2 mm and the corresponding **d** to achieve the desired sensitivity was roughly calculated with an analytical model as explained in section 2.2. Subsequently, **d** was fine-tuned with a step size of 5 µm using MCS (see section 2.3) to match the sensitivity exactly.
iii. The combinations of **h** and **d**, each defining a unique collimator, were used to create complete multi-pinhole collimators with the pinhole projections illustrated in figure 3. The pinholes were distributed into rings, and in each ring, the axes between adjacent pinholes made an angle equal to the pinhole opening angle. The angular shift between adjacent rings was half the pinhole opening angle. The distances between the rings were set manually.
iv. The collimators were then evaluated at fixed S_{CFOV} based on full image reconstruction of a Derenzo phantom with a realistic activity concentration of ^{18}F (described in section 2.5.2). For each S_{CFOV}, the value of **h** that results in the reconstructed Derenzo image with the highest contrast-to-noise ratio (CNR, equation (5)) was selected.
v. For each S_{CFOV} with the chosen set of **h** and **d**, the wall thickness **T** was reduced from 60 mm to 50 mm, 43 mm, and 30 mm to see which thickness still maintains good reconstructed image quality. To this end, we simulated both a Derenzo phantom and a uniform phantom (described in section 2.5.3) with a realistic ^{18}F activity concentration. The image quality was based on visual assessment, and quantitative metrics (CNR calculation for the Derenzo phantom, and portion of reconstructed activity present outside the uniform phantom).
vi. Finally, we obtained an optimised collimator for each S_{CFOV}, defined by a set of **h, d**, and **T**, and the estimated collimator weights, as well as the updated sensitivities for the finally chosen wall thickness, were recorded.

Subsequently, two collimator designs selected for the two considered sensitivities were evaluated with high concentrations of ^{18}F and biologically realistic activities of some other high-energy isotopes, namely ^{64}Cu, ^{124}I, ^{213}Bi, and ^{131}I, to see which spatial resolution can be achieved. For comparison, simulations with an *in vivo* collimator in the VECTor system (Goorden *et al* 2013) having a pinhole diameter of 0.7 mm (dubbed HE-UHR-M by MILabs B.V.) were added to see how much resolution gain the new EXIRAD-HE collimators offers.

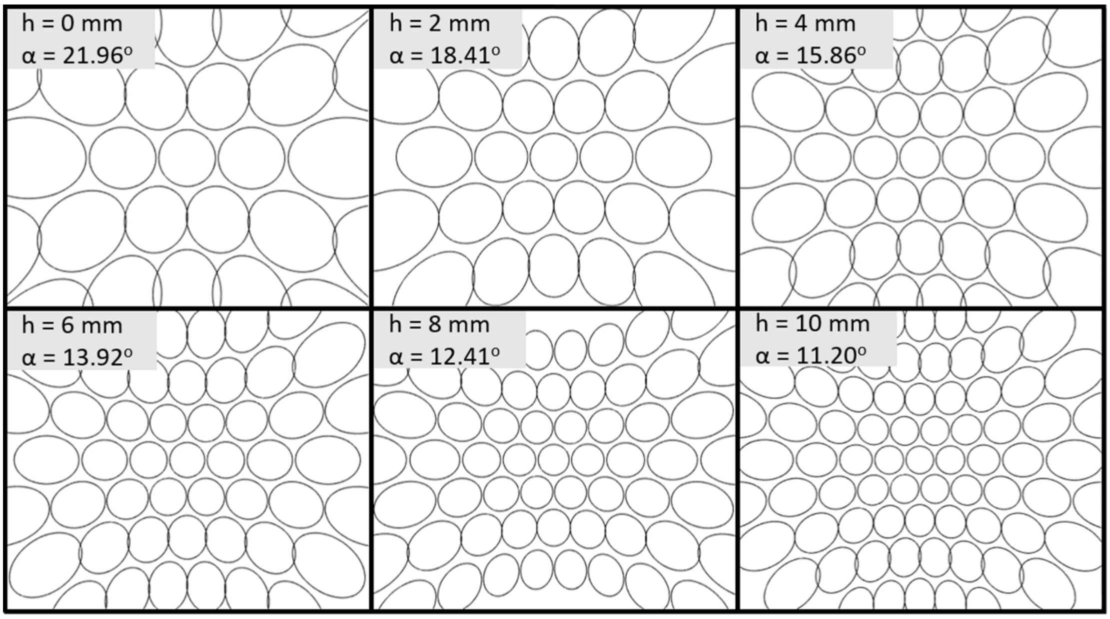

Figure 3. Geometric projection on one of the detectors with the manually placed pinholes for varying distance from pinhole centres to the collimator inner surface (**h**). The indicated opening angle for each **h** is for the pinholes in middle rings. The opening angle of the pinholes in the two outermost rings is two degrees smaller than that to prevent projection overlapping.

Furthermore, a digital mouse knee joint phantom and a digital tumour xenograft phantom (described in section 2.5.4) were simulated to evaluate the collimators' performance in tissue scans. The reconstructed images with the new collimators were also compared with those obtained with the VECTor collimator and 1 mm blurred images of the original activity distribution that represents typical images of commercial coincidence PET.

2.5. Image reconstruction

2.5.1. General settings

All studied scans were simulated with MCS. In each scan, the object was placed at multiple bed positions and the projections acquired from all bed positions were used together in image reconstruction (Vastenhouw and Beekman 2007). For image reconstruction, a system matrix was generated for each of the investigated collimators, using the ray-tracing method as described in (Goorden *et al* 2016). In this method, the system matrix was calculated given the position and orientation of the collimators and detectors, as well as the energy-dependent linear attenuation coefficients of the collimator and detector materials. The system matrix for each isotope was generated at the energy of the chosen photopeak (table 2). To keep a reasonable matrix size and reconstruction time, only the gamma photon paths that have a probability of at least 1% to pass through the collimator material are included into the system matrix. Reconstructions were performed using the similarity-regulated ordered-subset expectation maximisation (SROSEM) algorithm (Vaissier *et al* 2016). Post-filtering was applied with the filter size indicated for each phantom in sections 2.5.2–2.5.4. Images were reconstructed on an isotropic 0.25 mm voxel grid. Scatter and background radiation were corrected using the triple-energy window method (Ogawa *et al* 1991) with two side windows adjacent to the photopeak, each having a width of 25% of the photopeak window's width. Positron range was corrected by including it in the forward step of the reconstruction using pre-calculated kernels (Goorden *et al* 2016). Note that positron range correction was not applicable for ^{124}I, ^{213}Bi, and ^{131}I for the corresponding acquired photopeaks.

2.5.2. Digital derenzo phantoms

Two Derenzo phantoms simulated in this work are shown in figure 4. Derenzo phantom 1 was used most of the time, and Derenzo phantom 2 was only for the ^{131}I scan in figure 7 to show smaller rods. Each phantom has six sectors, in each of which, the distance between centres of two adjacent rods was twice the rod diameter. The whole phantom was placed at the centre of a PMMA cylinder having a diameter of 14 mm and a length of 8 mm.

Various activities in the phantoms and scan times were assumed for the collimator optimisation and evaluation. We simulated biologically realistic activity concentration in mice of ^{18}F (4.39 MBq ml^{-1}), ^{64}Cu (9 MBq ml^{-1}), ^{124}I (9.6 MBq ml^{-1}), ^{213}Bi (12.4 MBq ml^{-1}), ^{131}I (54 MBq ml^{-1}) that were retrieved from (Laitinen *et al* 2006, Lee *et al* 2010, Senekowitsch-Schmidtke *et al* 2001, Nomura *et al* 2014, and

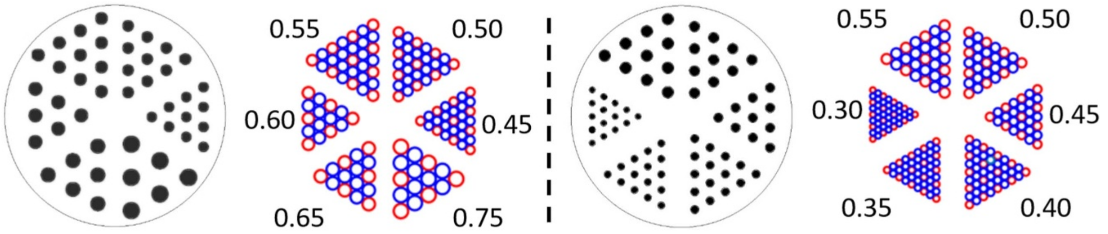

Figure 4. Derenzo phantoms with rod diameters in mm and the regions of interest for the CNR calculation. (a) Derenzo phantom 1. (b) Derenzo phantom 2.

Table 3. The obtained values of **d** (in mm) to achieve the desired system sensitivities and the CNRs from three realisations, represented as mean ± standard deviation, for the corresponding values of **h.**

h (mm)		2	4	6	**8**	10
$S_{\mathrm{CFOV}} = 0.30\%$	**d** (mm)	N/A	N/A	0.160	**0.270**	0.305
	CNR			0.96 ± 0.04	$\mathbf{1.77 \pm 0.06}$	1.10 ± 0.04
$S_{\mathrm{CFOV}} = 0.60\%$	**d** (mm)	0.135	0.385	0.505	**0.595**	0.620
	CNR	0.50 ± 0.07	1.38 ± 0.04	1.77 ± 0.06	$\mathbf{2.02 \pm 0.05}$	1.96 ± 0.03

Table 4. A_{outside} stands for the percentage of reconstructed activity outside uniform phantom relative to the total activity. Note that the listed sensitivities are for **T** = 60 mm.

T (mm)		30	**43**	50	60
$S_{\mathrm{CFOV}} = 0.30\%$	CNR	1.58 ± 0.02	$\mathbf{1.52 \pm 0.07}$	1.59 ± 0.26	1.77 ± 0.06
	A_{outside}	26.7%	**15.6%**	13.6%	10.3%
$S_{\mathrm{CFOV}} = 0.60\%$	CNR	1.88 ± 0.01	$\mathbf{1.92 \pm 0.18}$	1.93 ± 0.11	2.02 ± 0.05
	A_{outside}	18.8%	**12.6%**	11.0%	9.1%

van der Have *et al* 2016), respectively. Higher ^{18}F activities (20 MBq ml^{-1} and 60 MBq ml^{-1}), which can be of interest in *ex vivo* imaging, were also tested. The scan time was set to 4 h for ^{18}F, 1 h for ^{213}Bi, and 16 h for ^{64}Cu, ^{124}I, and ^{131}I considering the isotopes' half-lives (see table 2).

Data acquisition with sixteen bed positions was simulated for this phantom. The images that were shown had the iteration number and the 3D Gaussian post-filter that maximised the CNR. The CNR was calculated in the same way as in (Walker *et al* 2014). For this purpose, we drew the activity regions (red circle) and the background regions (blue circles) as indicated in figure 4 that span a depth of 1.5 mm (or six slices). CNR was defined as:

$$\mathrm{CNR} = \frac{1}{n_s} \sum_s \frac{\overline{I_s} - \overline{B_s}}{\overline{I_s}} / \frac{\sqrt{\sigma^2_{I_{s,p}} + \sigma^2_{B_{s,p}}}}{\overline{IB_s}}, \tag{5}$$

where $\overline{I_s}$ and $\overline{B_s}$ are the mean intensity over the activity regions and the background regions of sector s, respectively. $\sigma_{I_{s,p}}$ and $\sigma_{B_{s,p}}$ are standard deviations over these regions, calculated on a subset of planes p, $p \in \{1, 3, 5\}$ to reduce covariance between planes. $\overline{IB_s}$ is mean intensity over all regions of interest in sector s, and n_s is the number of rod sectors. For EXIRAD-HE, all sectors were included, while for VECTor, only the three largest sectors were used in CNR calculation because the smaller sectors were not well resolved. The CNR's mean and standard deviation reported in tables 3 and 4 were calculated with three noise realisations, while the CNR for figure 7 was from one realisation.

2.5.3. Digital uniform phantom

To study the wall thickness, a uniformly filled syringe (6.5 mm inner diameter and 10 mm length) was simulated. The whole phantom was placed at the centre of a PMMA cylinder having a diameter of 14 mm and a length of 14 mm. The phantom was assumed to contain 4.39 MBq ml^{-1} ^{18}F and to have been scanned for 4 h. Forty-five bed positions were used for this phantom. All the uniform phantom images were shown at the 10th iteration with the same post-reconstruction filters, a 0.7 mm FWHM 3D Gaussian filter followed by a 7*7*7-voxels Median filter. Reconstructed image quality was evaluated based on visual assessment and the percentage of activity reconstructed outside the phantom.

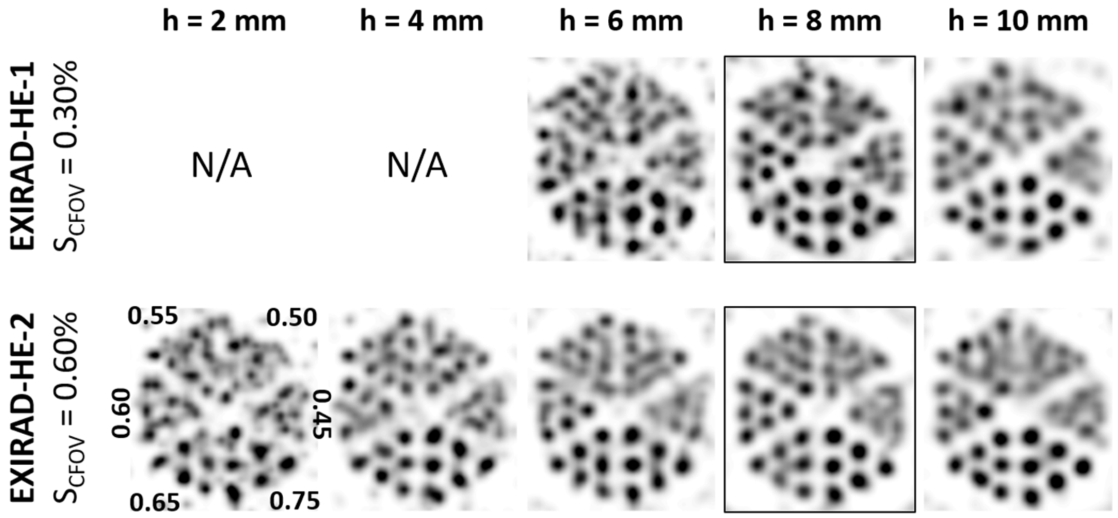

Figure 5. Images of Derenzo phantom 1 filled with 4.39 MBq ml^{-1} ^{18}F and scanned for 4 h for the optimisation of **h** and **d**. Each image was obtained with one collimator and displayed with the iteration and the 3D Gaussian filter size that maximises the CNR. The optimal image for each sensitivity is enclosed in a square box. Slice thickness was 1.5 mm.

2.5.4. Digital mouse tissue phantoms

A mouse knee joint phantom was derived from a real 3D image of a mouse knee joint containing ^{99m}Tc-methylene diphosphonate (^{99m}Tc-MDP) scanned with the low-energy EXIRAD collimator, and here assumed to contain ^{18}F-Na as these isotopes label the same target in the bone. The mouse knee joint contained 56 MBq ml^{-1} ^{18}F (obtained from experimental data with ^{18}F) and has been scanned for 4 h. This phantom volume had a size of 4.45*4.45*6.45 mm^{3,} and three bed positions were used.

Furthermore, a tumour xenograft phantom consisting of a large tumour with a necrotic core, and two small spherical tumours next to each other was simulated to contain ^{131}I-NaI. The mouse was assumed to be injected with 20 MBq ^{131}I and 10.2% ID/g was on the tumour at the time of termination (Tijink *et al* 2009). The xenograft was presumed to be snap-frozen and imaged for 16 h. This phantom volume had a size of 6.25*6.25*6.25 mm^{3,} and five bed positions were used.

In both cases, the reconstructed images were displayed at the iteration number and the 3D Gaussian filter size that yielded the lowest normalised mean-squared error (NMSE) and evaluated based on both visual assessment and NMSE.

3. Results

3.1. Collimator optimisation

Figure 5 compares reconstructed images of Derenzo phantom 1 when varying **h**. The pinhole diameters **d** that result in the desired system sensitivities and the image CNRs are reported in table 3. 'N/A' represents the case in which no non-negative value of **d** can be found to achieve the target S_{CFOV}. This was also the case when setting **h** = 0 mm. For both sensitivity levels, **h** = 8 mm offered the images with the highest CNR and was hence selected.

Figure 6 shows the reconstructed images of Derenzo phantom 1 and the uniform phantom when varying wall thickness, and table 4 presents the corresponding CNRs of the Derenzo images as well as the percentage of activity reconstructed outside the uniform. Visual assessment on the Derenzo phantom's rods and on the activity within the uniform phantom volume does not show significant image degradation as the wall thickness reduces from 60 mm to 30 mm. However, the artefacts outside the uniform phantom do increase, especially for the 30 mm thick collimator. Table 4 indicates that as the collimator wall gets thinner, the CNR decreases and the activity reconstructed outside the uniform phantom increases with the most degradation when going from 43 mm to 30 mm. Therefore, we chose **T** = 43 mm to keep a reasonable collimator weight of 16 kg for the core. The weight variation between the collimators for the two sensitivities is negligible because only pinhole diameters change (0.270 mm versus 0.595 mm).

Table 5 presents the final parameters of the two optimal collimators, EXIRAD-HE-1 and EXIRAD-HE-2, with reference to the VECTor collimator. It turns out that EXIRAD-HE-1 and EXIRAD-HE-2 are only different in the pinhole diameter, which leads to the different system sensitivities. The listed sensitivities of the EXIRAD-HE collimators here were calculated with ^{18}F and the chosen wall thickness (**T** = 43 mm), which are now slightly higher than the initially targeted sensitivities set at the beginning of the optimisation process.

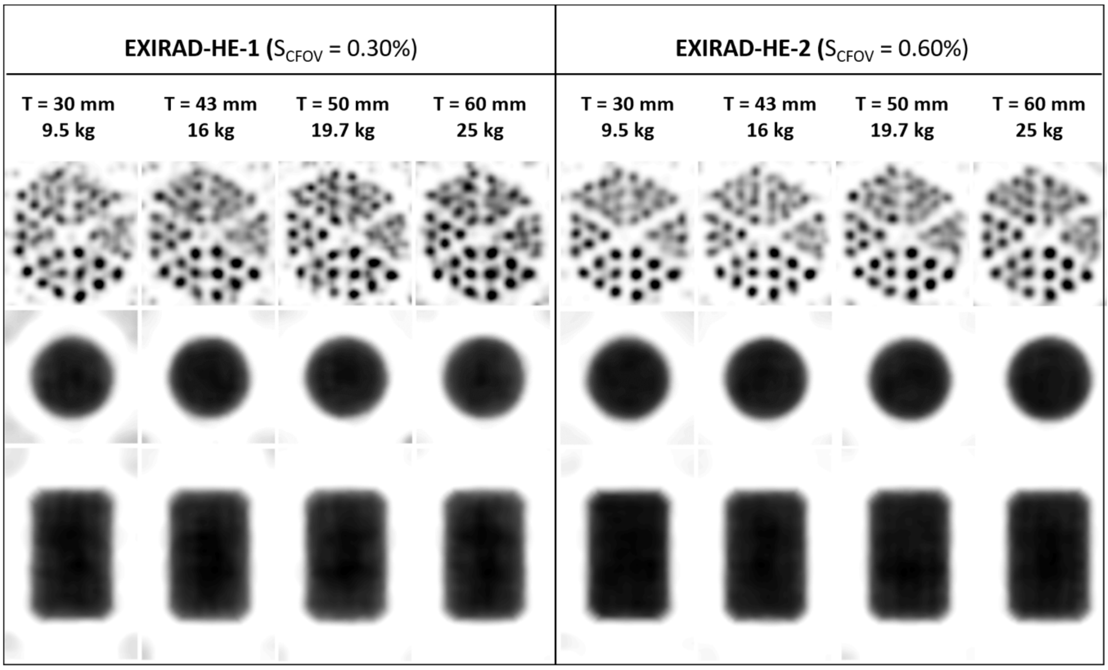

Figure 6. Reconstructed images of the Derenzo phantom 1 and the uniform phantom, both filled with 4.39 MBq ml^{-1} ^{18}F and scanned for 4 h, for the optimisation of **T**. Here the value of **h** was already fixed to 8 mm. Note that the listed sensitivities are only for **T** = 60 mm and we would expect slightly higher sensitivities for the smaller wall thicknesses. The Derenzo images were displayed with the iteration and the 3D Gaussian filter size that maximises the CNR. All the uniform phantom images were shown at the 10th iteration with the same post-reconstruction filters, 0.7 mm FWHM 3D Gaussian filter + 7*7*7-voxels Median filter. Slice thickness was 1.5 mm.

Table 5. Parameters of the selected EXIRAD-HE collimators and reference to the HE-UHR-M collimator in VECTor which was also simulated in this paper for comparison. For each collimator, two angles are listed: the larger one is for the inner rings, and the smaller one is for the two outermost rings near two ends of the collimator.

	EXIRAD-HE-1	EXIRAD-HE-2	VECTor
S_{CFOV} (%)	0.312	0.617	0.30
r_f (mm)	2	2	6
h (mm)	8	8	8
d (mm)	0.270	0.595	0.70
T (mm)	43	43	43
α (degree)	12.41, 10.41	12.41, 10.41	18, 16
N	177	177	162
Number of rings	7 rings	7 rings	4 clustered-rings

3.2. Evaluation with digital derenzo phantoms

Figure 7 displays simulated images of the Derenzo phantoms filled with ^{18}F at several activity concentrations as well as some other high-energy isotopes using the optimal collimators. These reconstructed images are placed next to the images obtained with the *in vivo* collimator in VECTor to see the benefit of the new *ex vivo* collimator. Each column corresponds to a scan with a fixed setup, and only the collimator is changed. The image that shows the clearest rods in each scan is enclosed in a box. Here only the scans with ^{131}I used the smaller phantom, Derenzo phantom 2, to visualise rods with smaller sizes.

In all of the investigated scans, the two EXIRAD-HE collimators clearly offer better images than the VECTor collimator. Comparing between EXIRAD-HE-1 and EXIRAD-HE-2, in some scans, the higher-sensitivity collimator performs better, while in the other scans the lower-sensitivity design offers superior images. That is understandable since, with relatively low radioactivity, we would choose a high-sensitivity collimator to acquire more counts that benefit image quality, and if the radioactivity is already relatively high, a high-resolution collimator will offer a better image resolution.

The achievable spatial resolutions, defined by the diameters of the smallest visible rods, are 0.5 mm, 0.6 mm, 0.5 mm, 0.6 mm, and 0.35 mm for ^{18}F, ^{64}Cu, ^{124}I, ^{213}Bi, and ^{131}I imaging, respectively.

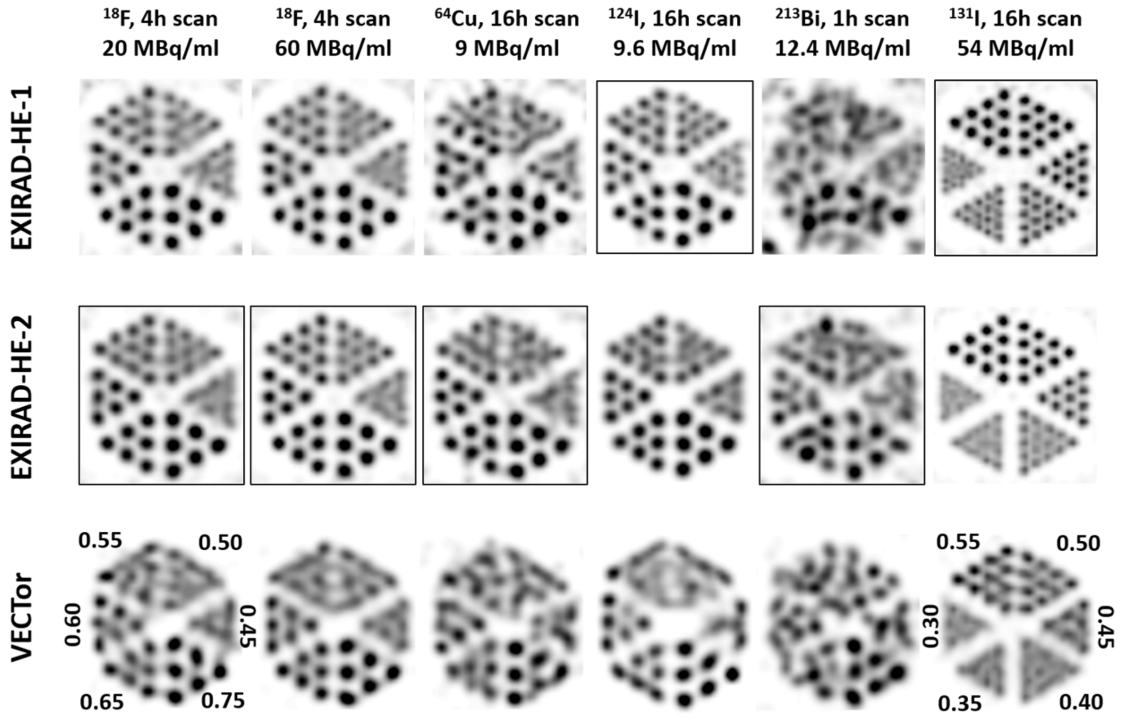

Figure 7. Simulated images of the Derenzo phantoms with ^{18}F at several activity levels as well as with some other high-energy isotopes using the optimal collimators in table 5. Only the ^{131}I scan (rightmost column) was simulated with a smaller Derenzo phantom to visualise rods with smaller diameters. The images were displayed with the iteration and the 3D Gaussian filter size that maximises CNR. However, maximising CNR was visually suboptimal for ^{213}Bi and ^{131}I scans with EXIRAD-HE, so the iteration number and the filter size were chosen manually for these cases. In each column, the performance of the three collimators is compared, and the image that shows the clearest rods is enclosed in a square box. Slice thickness was 1.5 mm.

3.3. Evaluation with digital mouse tissue phantoms

Figures 8 and 9 demonstrate the performance of the new collimators in imaging a mouse knee joint containing ^{18}F-NaF, and a tumour xenograft containing ^{131}I-NaI, respectively. In both cases, EXIRAD-HE resolves more details than VECTor. The xenograft image obtained with the VECTor collimator shows a smaller necrotic core of the central tumour than the actual shape, an unclear separation between the central tumour and the smaller tumours, and the invisibility of the smallest tumour. With the EXIRAD-HE collimators, the whole reconstructed shape of the xenograft is very close to that of the true phantom, and each of the tumours can be recovered with great detail. EXIRAD-HE-1 performs better than EXIRAD-HE-2 in the knee joint scan, while EXIRAD-HE-2 yields an image with clearer shape of the tumours than EXIRAD-HE-1 does in the xenograft scan. These results agree with the NMSE as reported in figures 8 and 9's legends. In both cases, the 1 mm blurred images of the phantom offer significantly less detail than the images with EXIRAD-HE and VECTor.

4. Discussion

We have introduced two multi-pinhole collimators for *ex vivo* imaging of high-energy isotopes. Both collimators have shown, in various simulated scans, superior image resolution to the *in vivo* multi-pinhole SPECT/PET. The new collimators yielded a resolution of 0.5 mm, 0.6 mm, 0.5 mm, 0.6 mm, and 0.35 mm for ^{18}F, ^{64}Cu, ^{124}I, ^{213}Bi, and ^{131}I, respectively at realistic activity concentration levels. We believe that these resolution gains are important in many applications. For example, in a mouse scan with Fluorodeoxyglucose to detect the reduction in posterior cingulate activity—a sign for Alzheimer's disease, a resolution of 0.5 mm is on the verge of being possible to detect this effect, and a resolution of 0.75 mm or worse fails to detect significantly abnormal activity (Valla *et al* 2002). Besides, the 1 mm resolution images presented in figures 8 and 9 emphasise that sub-mm resolutions can reveal a lot of extra details.

These achievable resolutions with EXIRAD-HE for the PET isotopes ^{18}F and ^{64}Cu are probably already near the fundamental limit because of the positron range effect (Levin and Hoffman 1999). The average positron ranges of ^{18}F and ^{64}Cu in water are 0.64 mm and 0.56 mm, respectively (Cal-González *et al* 2013). This effect is not present if we utilise prompt gammas from non-pure positron emitters or single gammas from isotopes like ^{213}Bi or ^{131}I for imaging; therefore, EXIRAD-HE is most suitable for such isotopes.

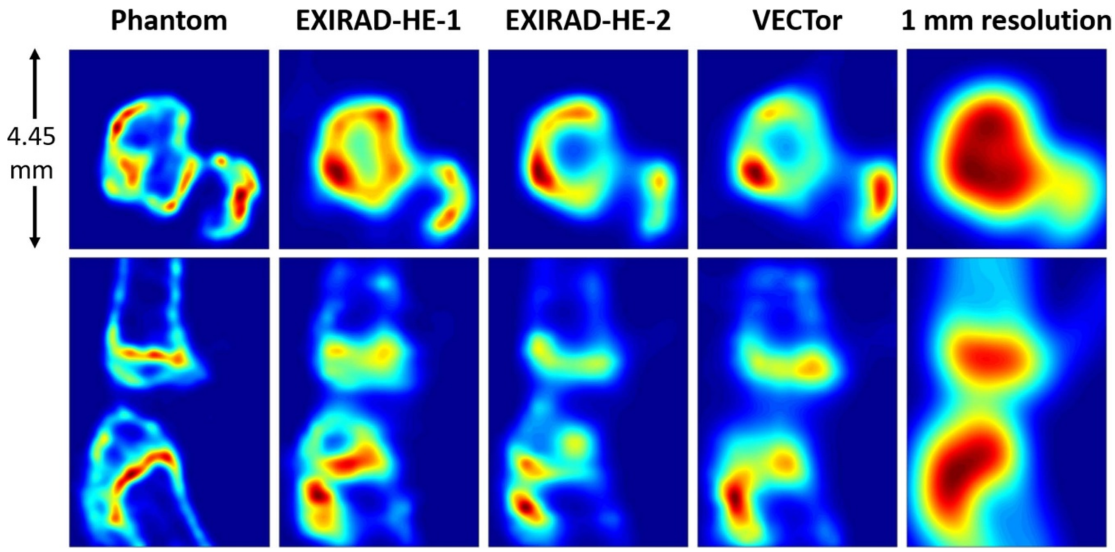

Figure 8. Simulation of a mouse knee joint phantom with the optimal collimators (table 5) in comparison with the HE-UHR-M collimator in VECTor and the 1 mm blurred image of the phantom. The images are shown at the iteration number that gives the lowest NMSE. The optimal NMSE is 0.17, 0.18, and 0.25 for EXIRAD-HE-1, EXIRAD-HE-2, and VECTor, respectively. Slice thickness was 0.5 mm.

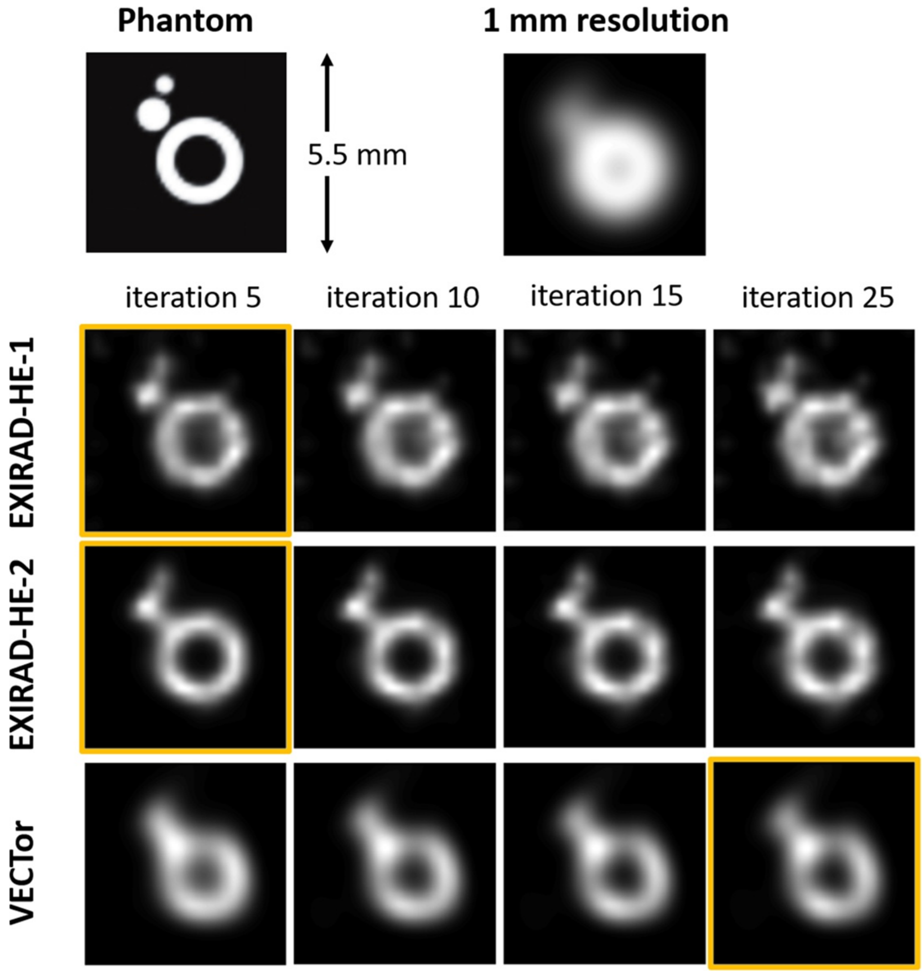

Figure 9. Simulation of a mouse tumour xenograft phantom with the optimal collimators (table 5) in comparison with the HE-UHR-M collimator in VECTor and the 1 mm blurred image of the phantom. Images are shown at several iteration numbers, and the images with the lowest NMSE are enclosed in boxes. The optimal NMSE is 0.05, 0.03, and 0.12 for EXIRAD-HE-1, EXIRAD-HE-2, and VECTor, respectively. Slice thickness was 0.5 mm.

Besides, for sufficiently long half-life isotopes, the scan duration could be extended as the tissue sample is kept frozen over the course of the scan for good image quality.

Considering the manufacturing feasibility, the proposed EXIRAD-HE collimators only consist of round pinholes with no shielding outside as is present for the low-energy EXIRAD collimator (Nguyen *et al* 2019). Adding a trapezium-hole shielding, we would be able to place the pinholes of the same opening angle slightly tighter, which translates into more pinholes without the cost of projection overlapping. Even though each pinhole will be truncated, the overall system sensitivity is expected to slightly increase for the same system resolution. However, the manufacturing complexity and cost will increase significantly because of the large number of narrow trapezium holes in this shielding.

As seen in figures 7–9, each of the two proposed collimators has certain advantages, and the choice between them depends on the imaging situation. For relatively low activity levels, one may prefer the higher-sensitivity collimator for higher counts whereas when the count level is sufficient, the lower-sensitivity collimator would be selected for optimal image resolution.

5. Conclusion

This paper presented the design, optimisation, and evaluation of new multi-pinhole collimators for *ex vivo* 3D tomographic imaging of high-energy isotopes. We found that placing pinhole centres at a distance of 8 mm from the collimator inner surface yielded optimal image resolution for fixed system sensitivity over the CFOV. A wall thickness of 43 mm that keeps a reasonable weight (16 kg for the core) still maintains excellent image quality compared to a wall thickness of 60 mm (25 kg for the core). With the two optimal high-energy collimators, the system offers a resolution of 0.35 mm, 0.6 mm, 0.5 mm, 0.6 mm, and 0.5 mm when imaging ^{131}I, ^{213}Bi, ^{18}F, ^{64}Cu, and ^{124}I, respectively, contained in tissue samples.

Acknowledgments

The authors would like to thank Ruud Ramakers (MILabs B.V.) for providing the experimental activity concentration of ^{18}F-Na in the mouse knee, and the background radiation measurement data.

ORCID iD

Minh Phuong Nguyen https://orcid.org/0000-0001-6114-5682

References

Beekman F J, Kamphuis C, Koustoulidou S, Ramakers R M and Goorden M C 2020 Positron range-free and multi-isotope tomography of positron emitters *Nat. Meth.* submitted

Beekman F J, Kamphuis C, Koustoulidou S, Vastenhouw B, Rendon D, Ramakers R M, Blazis S, van Cauter S, Goorden M C and Gremse F 2018 VECTor-6: broadband photon tomography takes the versatility of multi-modality preclinical imaging beyond the limits of PET-SPECT-CT and optical imaging *WMIC 2018 Seattle, USA*

Beekman F J, van der Have F, Vastenhouw B, van der Linden A J A, van Rijk P P, Burbach J P H and Smidt M P 2005 U-SPECT-I: a novel system for submillimeter-resolution tomography with radiolabeled molecules in mice *J. Nucl. Med.* **46** 1194–200

Cal-González J, J L H, España S, Corzo P M G, Vaquero J J, Desco M and Udias J M 2013 Positron range estimations with PeneloPET *Phys. Med. Biol.* **58** 5127–52

Chen C L, Wang Y, Lee J J S and Tsui B M W 2008 Integration of SimSET photon history generator in GATE for efficient Monte Carlo simulations of pinhole SPECT *Med. Phys.* **35** 3278–84

Crawford J R, Robertson A K H, Yang H, Rodríguez-Rodríguez C, Esquinas P L, Kunz P, Blinder S, Sossi V, Schaffer P and Ruth T J 2018 Evaluation of ^{209}At as a theranostic isotope for ^{209}At-radiopharmaceutical development using high-energy SPECT *Phys. Med. Biol.* **63** 045025

de Swart J, Chan H S, Goorden M C, Morgenstern A, Bruchertseifer F, Beekman F J, de Jong M and Konijnenberg M W 2016 Utilizing high-energy γ-photons for high-resolution 213Bi SPECT in mice *J. Nucl. Med.* **57** 486–92

Gonzalez A J *et al* 2016 Next generation of the Albira small animal PET based on high density SiPM arrays *2015 IEEE Nuclear Science Symp. and Medical Imaging Conf., NSS/MIC 2015* (Institute of Electrical and Electronics Engineers Inc.) (https://doi.org/10.1109/NSSMIC.2015.7582085)

Goorden M C, Rentmeester M C M and Beekman F J 2009 Theoretical analysis of full-ring multi-pinhole brain SPECT *Phys. Med. Biol.* **54** 6593–610

Goorden M C, van der Have F, Kreuger R, Ramakers R M, Vastenhouw B, Burbach J P H, Booij J, Molthoff C F M and Beekman F J 2013 VECTor: A Preclinical Imaging System for Simultaneous Submillimeter SPECT and PET *J. Nucl. Med.* **54** 306–12

Goorden M C, van Roosmalen J, van der Have F and Beekman F J 2016 Optimizing modelling in iterative image reconstruction for preclinical pinhole PET *Phys. Med. Biol.* **61** 3712–33

Herrmann K, Dahlbom M, Nathanson D, Wei L, Radu C, Chatziioannou A and Czernin J 2013 Evaluation of the genisys4, a bench-top preclinical PET scanner *J. Nucl. Med.* **54** 1162–7

Hubbell J H and Seltzer S M 1995 Tables of x-ray mass attenuation coefficients and mass energy-absorption coefficients Online: http://physics.nist.gov/PhysRefData/XrayMassCoef/cover.html

Ivashchenko O, van der Have F, Villena J L, Groen H C, R M R, Weinans H H and Beekman F J 2014 Quarter-millimeter-resolution molecular mouse imaging with U-SPECT$^+$ *Mol. Imaging* **13** 1–8

Jan S *et al* 2011 GATE V6: a major enhancement of the GATE simulation platform enabling modelling of CT and radiotherapy *Phys. Med. Biol.* **56** 881–901

Jan S *et al* 2004 GATE: a simulation toolkit for PET and SPECT *Phys. Med. Biol.* **49** 4543

Krishnamoorthy S, Blankemeyer E, Mollet P, Surti S, Van Holen R and Karp J S 2018 Performance evaluation of the MOLECUBES β-CUBE - A high spatial resolution and high sensitivity small animal PET scanner utilizing monolithic LYSO scintillation detectors *Phys. Med. Biol.* **63** 155013

Laitinen I *et al* 2006 Non-specific binding of [18F]FDG to calcifications in atherosclerotic plaques: experimental study of mouse and human arteries *Eur. J. Nucl. Med. Mol. Imaging* **33** 1461–7

Lee C-L *et al* 2010 Radiation dose estimation using preclinical imaging with 124 I-metaiodobenzylguanidine (MIBG) PET *Med. Phys.* **37** 4861

Levin C S and Hoffman E J 1999 Calculation of positron range and its effect on the fundamental limit of positron emission tomography system spatial resolution *Phys. Med. Biol.* **44** 781

Metzler S D, Bowsher J E, Smith M F and Jaszczak R J 2001 Analytic determination of pinhole collimator sensitivity with penetration *IEEE Trans. Med. Imaging* **20** 730–41

Nguyen M P, Goorden M C, Kamphuis C and Beekman F J 2019 Evaluation of pinhole collimator materials for micron-resolution ex vivo SPECT *Phys. Med. Biol.* **64** 105107

Nguyen M P, Ramakers R M, Kamphuis C, Koustoulidou S, Goorden M C and Beekman F J 2020 EXIRAD-3D: fast automated three-dimensional autoradiography *Nucl. Med. Biol.* **86–87** 59–65

Nomura S *et al* 2014 PET imaging analysis with 64 Cu in disulfiram treatment for aberrant copper biodistribution in menkes disease mouse model *J. Nucl. Med.* **55** 845–51

Ogawa K, Harata Y, Ichihara T, Kubo A and Hashimoto S 1991 A practical method for position-dependent compton-scatter correction in single photon emission CT *IEEE Trans. Med. Imaging* **10** 408–12

Rentmeester M C M, van der Have F and Beekman F J 2007 Optimizing multi-pinhole SPECT geometries using an analytical model *Phys. Med. Biol.* **52** 2567–81

Rowland D J and Cherry S R 2008 Small-animal preclinical nuclear medicine instrumentation and methodology *Semin. Nucl. Med.* **38** 209–22

Sato K *et al* 2016 Performance evaluation of the small-animal PET scanner ClairvivoPET using NEMA NU 4–2008 standards *Phys. Med. Biol.* **61** 696–711

Seltzer S M 1993 Calculation of photon mass energy-transfer and mass energy-absorption coefficients *Radiat. Res* **136** 147

Senekowitsch-Schmidtke R *et al* 2001 Highly specific tumor binding of a 213Bi-labeled monoclonal antibody against mutant E-cadherin suggests its usefulness for locoregional alpha-radioimmunotherapy of diffuse-type gastric cancer *Cancer Res.* **61** 2804–8

Staelens S, Vunckx K, De Beenhouwer J, Beekman F, Asseler Y D, Nuyts J and Lemahieu I 2006 GATE simulations for optimization of pinhole imaging *Nucl. Instrum. Meth. Phys. Res.* A **569** 359–63

Tijink B M, Perk L R, Budde M, Stigter-Van Walsum M, Visser G W M, Kloet R W, Dinkelborg L M, Leemans C R, Neri D and Van Dongen G A M S 2009 124I-L19-SIP for immuno-PET imaging of tumour vasculature and guidance of 131I-L19-SIP radioimmunotherapy *Eur. J. Nucl. Med. Mol. Imaging* **36** 1235–44

Vaissier P E B, Beekman F J and Goorden M C 2016 Similarity-regulation of OS-EM for accelerated SPECT reconstruction *Phys. Med. Biol.* **61** 4300–15

Valla J, Chen K, Berndt J D, Gonzalez-Lima F, Cherry S R, Games D and Reiman E M 2002 Effects of image resolution on autoradiographic measurements of posterior cingulate activity in PDAPP mice: implications for functional brain imaging studies of transgenic mouse models of Alzheimer's disease *Neuroimage* **16** 1–6

van der Have F, Ivashchenko O, Goorden M C, Ramakers R M and Beekman F J 2016 High-resolution clustered pinhole 131Iodine SPECT imaging in mice *Nucl. Med. Biol.* **43** 506–11

Vastenhouw B and Beekman F 2007 Submillimeter total-body murine imaging with U-SPECT-I *J. Nucl. Med.* **48** 487–93

Walker M D, Goorden M C, Dinelle K, Ramakers R M, Blinder S, Shirmohammad M, van der Have F, Beekman F J and Sossi V 2014 Performance assessment of preclinical PET scanner with pinhole collimation by comparison to a coincidence-based small-animal-PET scanner *J. Nucl. Med.* **55** 1368–74

Yang Y *et al* 2016 A high resolution prototype small-animal PET scanner dedicated to mouse brain imaging *J. Nucl. Med.* **57** 1130–5